Probing equilibrium of molecular and deprotonated water on TiO_2(110)

Zhi-Tao Wang[a,b,1], Yang-Gang Wang[b,c,1], Rentao Mu[b,c,1], Yeohoon Yoon[b,c], Arjun Dahal[a,b], Gregory K. Schenter[b,d], Vassiliki-Alexandra Glezakou[b,c], Roger Rousseau[b,c,2], Igor Lyubinetsky[b,c,2,3], and Zdenek Dohnálek[b,c,2]

[a]Microscopy Group, Environmental Molecular Sciences Laboratory, Pacific Northwest National Laboratory, Richland, WA 99352; [b]Institute for Integrated Catalysis, Pacific Northwest National Laboratory, Richland, WA 99352; [c]Catalysis Group, Physical Sciences Division, Physical and Computational Sciences Directorate, Pacific Northwest National Laboratory, Richland, WA 99352; and [d]Chemical Physics & Analysis Group, Physical Sciences Division, Physical & Computational Sciences Directorate, Pacific Northwest National Laboratory, Richland, WA 99352

Edited by Martin Gruebele, University of Illinois at Urbana–Champaign, Urbana, IL, and approved January 10, 2017 (received for review August 17, 2016)

Understanding adsorbed water and its dissociation to surface hydroxyls on oxide surfaces is key to unraveling many physical and chemical processes, yet the barrier for its deprotonation has never been measured. In this study, we present direct evidence for water dissociation equilibrium on rutile-TiO_2(110) by combining supersonic molecular beam, scanning tunneling microscopy (STM), and ab initio molecular dynamics. We measure the deprotonation/protonation barriers of 0.36 eV and find that molecularly bound water is preferred over the surface-bound hydroxyls by only 0.035 eV. We demonstrate that long-range electrostatic fields emanating from the oxide lead to steering and reorientation of the molecules approaching the surface, activating the O–H bonds and inducing deprotonation. The developed methodology for studying metastable reaction intermediates prepared with a high-energy molecular beam in the STM can be readily extended to other systems to clarify a wide range of important bond activation processes.

adsorbate dynamics | water | dissociative adsorption | titanium dioxide | kinetic barriers

Water is ubiquitous in the environment and, as such, the nature of its interactions with interfaces can determine the outcome of a broad range of processes that include wetting, dissolution, precipitation, phase transformation, corrosion, and catalytic and environmental reactions (1–7). In this regard, the relative stability of molecularly and dissociatively bound species can be of critical importance with the preferred configuration being controlled by many factors including surface structure, acid/base properties, defects, impurities, water coverage, and temperature (8–13). For oxides in particular, the relative stability of molecularly and dissociatively bound water has been widely debated even on the simplest, low-index surfaces.

Here we focus on resolving the fundamental question of water binding on rutile TiO_2(110), one of the most studied oxide surfaces, which is often used as a prototype for reducible oxide surfaces and a model for understanding photocatalytic water splitting (3, 14–17). Interestingly, despite the overwhelming wealth of literature, the nature of water adsorption and dissociation on nondefect titanium sites has been disputed for decades and to date remains unsettled (3, 14–17). The underpinning difficulty in resolving this debate is that it is practically impossible to prepare stoichiometric TiO_2(110) surfaces. As such, bridging hydroxyl groups formed by water dissociation in oxygen vacancy defects interfere with determining the extent of dissociation on regular Ti sites (3, 14–19). A number of recent studies by a variety of techniques including X-ray photoelectron spectroscopy (XPS) (20), infrared reflection absorption (21), photoelectron diffraction (PhD) (22), and scanning tunneling microscopy (STM) (23–25) arrived at conflicting conclusions. Whereas the XPS and PhD studies concluded partial dissociation of water in the hydrogen-bonded chains on Ti sites at higher coverages (20, 22), others are in favor of molecular bonding (21, 25).

To address the adsorption configuration of isolated water molecules, extremely low coverages are required. As such, the ensemble-averaged methods generally do not possess sufficient sensitivity and STM is the method of choice. Although the appearance of water-related features is suggestive of molecular binding, indirect evidence strongly indicates that water monomers can easily access the dissociated configuration (18, 19). For example, in the water-assisted diffusion of bridging hydroxyl hydrogen (18) and Ti-bound oxygen adatoms (19), water monomer dissociation represents a key step in the proposed mechanism. This is further supported by the wealth of theoretical studies that yield very close adsorption energies (within ∼0.1 eV) for molecularly and dissociatively bound water monomers (14–18).

To address this topic, we have constructed a unique instrument that allows for in situ molecular beam scattering studies directly under the STM tip, an instrument combination that has hitherto proven difficult to achieve (26–28). In this study, we used hyperthermal water beams with variable energy and probed the probability of the formation of metastable binding configurations on TiO_2(110) at low substrate temperatures (∼80 K). On metals, such molecular beam studies have proven indispensable for the understanding of dynamic factors controlling dissociation processes such as the excitation of vibrational modes, energy flow, and steering (29–31). We demonstrate that the observed metastable configurations are composed of terminal and bridging

Significance

Understanding how water binds and dissociates on surfaces has broad implications in a vast range of physical and chemical processes. The relative stability of molecularly and dissociatively bound water has been debated for decades on many oxide surfaces, but it has never been successfully measured. Our study describes unique instrumentation, direct measurements, and a state-of-the-art computation and theory approach that yield a detailed kinetic and dynamic description of water deprotonation equilibrium on TiO_2(110), a prototypical surface commonly used in mechanistic studies of photocatalytic water splitting. This unique study demonstrates that the molecularly bound water on TiO_2(110) is preferred over the surface-bound hydroxyls by only 0.035 eV.

Author contributions: G.K.S., R.R., I.L., and Z.D. designed research; Z.-T.W., Y.-G.W., R.M., Y.Y., A.D., and R.R. performed research; Y.-G.W., R.M., G.K.S., V.-A.G., R.R., I.L., and Z.D. analyzed data; and V.-A.G., R.R., I.L., and Z.D. wrote the paper.

The authors declare no conflict of interest.

This article is a PNAS Direct Submission.

[1]Z.-T.W., Y.-G.W., and R.M. contributed equally to this work.

[2]To whom correspondence may be addressed. Email: roger.rousseau@pnnl.gov, igor.lyubinetsky@oregonstate.edu, or zdenek.dohnalek@pnnl.gov.

[3]Present address: School of Chemical, Biological and Environmental Engineering, Oregon State University, Corvallis, OR 97331.

This article contains supporting information online at www.pnas.org/lookup/suppl/doi:10.1073/pnas.1613756114/-/DCSupplemental.

hydroxyl pairs that can be converted back to molecularly bound water at higher temperatures (>100 K). In parallel, theoretical protocols were developed to reveal mechanistic details, guide experiments, and provide data interpretation. We accurately determined the equilibrium distribution and the interconversion energy barriers. The analysis reveals that the dissociated water configuration is only 0.035 eV higher in energy. A unique finding of this study is that long-range (5–10-Å) electrostatic coupling between the incident molecules and the oxide surface results in a strong steering and reorientation before collision.

Results and Discussion

The STM images of clean TiO_2(110) composed of rows of topographically low-lying fivefold-coordinated titanium ions (Ti_{5c}, imaged bright) and high-lying bridging oxygen ions (O_b, imaged dark) are shown in Fig. 1 *A* and *C*. A small fraction of O_bs is missing, resulting in vacancies (V_Os) (15).

Fig. 1*B* shows the result after dosing H_2O with a room-temperature effusive molecular beam (incident energy of 0.06 eV) on the TiO_2(110) at 80 K. In all STM experiments, H_2O coverage was kept very low (~0.05 ML) to keep the observed molecules isolated. Only one type of feature, corresponding to water monomers centered on the Ti_{5c} rows (17, 18), is seen. Their uniformity is demonstrated in a high-contrast image (Fig. 1*B*, *Right*) and by the reproducibility of the line profiles (Fig. 1*B*, *Inset*, *Right*). Under limited surface mobility conditions (<160 K), the H_2O molecules do not diffuse on the Ti_{5c} rows on an experimentally observable timescale (24). As such, they are unable to reach V_O sites where they are known to dissociate and form bridging hydroxyl pairs (HO_bs) (3, 14, 15).

Whereas the H_2O features (Fig. 1*B*) are centered on Ti_{5c} sites, their appearance cannot be taken as conclusive evidence for the purely molecular binding of water. Under the equilibrium, $H_2O + O_b \rightleftarrows HO_t + HO_b$, where HO_t is the Ti_{5c}-bound terminal hydroxyl, the majority species (H_2O) determine the appearance. The evidence comes indirectly from studies of water reactions with O adatoms (19) and from water-assisted cross-row hydrogen transfer of HO_b species (18). Recent theoretical studies predict the higher stability of molecularly bound H_2O by less than 0.1 eV (13, 16–18).

We further probe the preparation of metastable species by colliding water molecules of high-incident energy (1.3 eV in Fig. 1*D*). In contrast to the low-incident energy experiment (Fig. 1*B*), two distinct types of features (65% H_2O and 35% P) are observed. The P features are round and also centered on Ti_{5c} sites. High contrast is needed (Fig. 1*D*, *Left*) to clearly discern their differences from H_2O. The line profiles in the inset further reveal that the P features are distinctly smaller and ~30% less intense than H_2O. Whereas in the area shown in Fig. 1*B* the P features are not present, they comprise ~5% of the total population at low H_2O incident energy. The large-scale images illustrating the overall distribution of the species at both low- and high-incident energies are shown in *SI Appendix*, section S1 and Fig. S1.

The appearance of the P features is surprising, as heuristically, pairs of two bright features (HO_t and HO_b) due to water dissociation are expected. To further interrogate the chemical makeup of the P species, we carry out temperature-dependent experiments for water with incident energy of 1.3 eV (Fig. 2). These experiments allow us to follow the thermal equilibration of the HO_t and HO_b species with H_2O.

In the first type of experiment, we image continuously the same area while the sample temperature is increased from 111 to 114 K (Fig. 2*A*). The conversion of one P feature (yellow circle) to H_2O (white circle) shows that the P features contain all of the atoms from the water molecule and that none of them has been irreversibly lost to the vacuum or subsurface. This evidence strongly supports that the P features comprise the HO_b/HO_t pairs. Additional evidence from tip-pulse manipulation experiments and STM image simulations is provided in *SI Appendix*, section S1 and Figs. S2–S4.

We quantify the temperature-dependent fraction of P features, $F_P(T)$, relative to the total number of H_2O + P features observed on the surface, $F_P(T)$, in Fig. 2*B* (circles). The initial H_2O adsorption temperature is stabilized between 80 and 150 K, water is dosed, and the surface is imaged. Below ~110 K, F_P remains approximately constant and equal to 0.35. Above 110 K, a sharp drop is detected and $T > 130$ K, F_P drops to 0.05 and remains approximately constant up to 150 K.

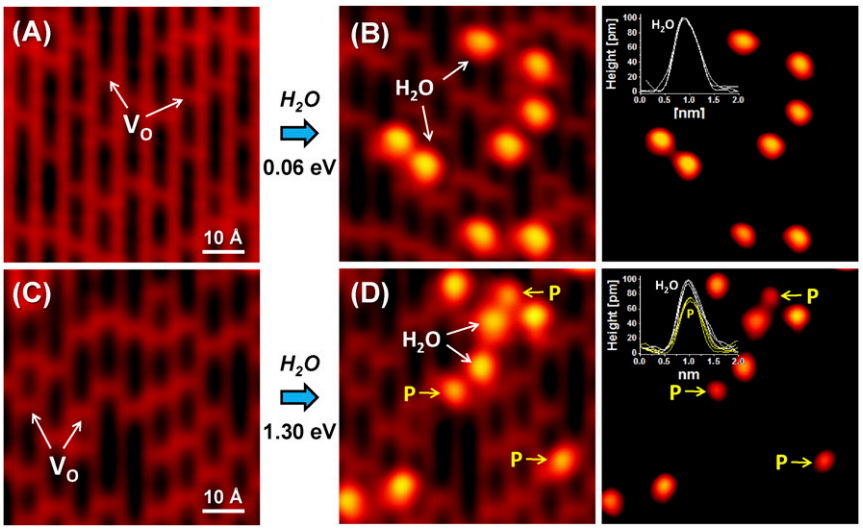

Fig. 1. Same area empty-state STM images before (*A* and *C*) and after (*B* and *D*) adsorption of 0.05 monolayer (ML) of water on TiO_2(110) at 80 K with the incident energy of 0.06 (*B*) and 1.30 eV (*D*). Images *A* and *C* show clean TiO_2(110) [Ti_{5c}, bright rows; O_b, dark rows; V_O defects (15%) appear as bright spots on dark O_b rows]. (*B*) A single type of features (labeled H_2O) is observed on Ti_{5c} rows at low-incident energy. A high-contrast image and the inset with three different line profiles along the Ti_{5c} rows in *B* (*Right*) highlight their uniformity. (*D*) Adsorption of the high-incident energy water (1.30 eV; *D*, *Left*) shows two types of features, H_2O and features labeled P. High-contrast image (*D*, *Right*) and the *Inset* further highlight their differences. The angle of incidence of the molecular beam is fixed at a polar angle of 60° with respect to the surface normal and azimuth pointing across the rows.

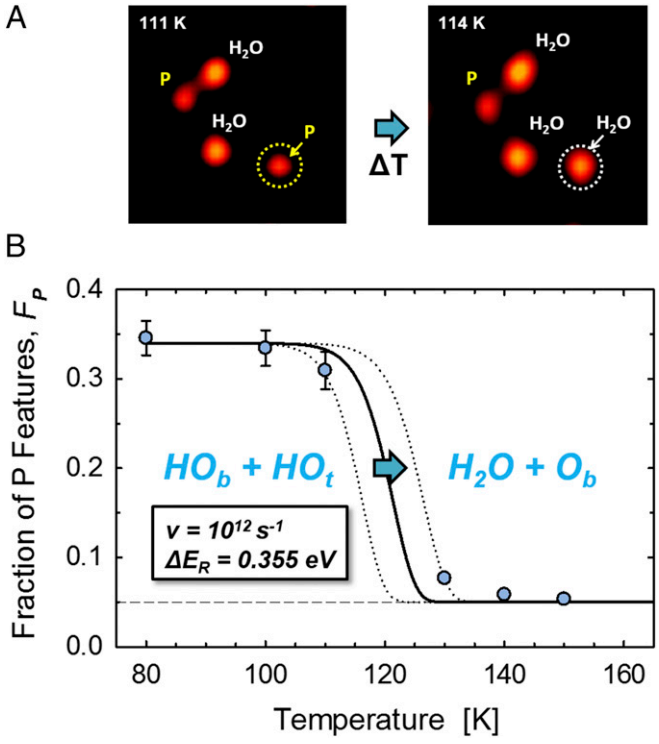

Fig. 2. (*A*) Thermally induced conversion of P features to H_2O following the adsorption of 0.05 ML of H_2O with incident energy of 1.3 eV. STM images (*Left*, T = 111 K; *Right*, 114 K) from an extended sequence obtained during the slow temperature ramp (0.1 K/min from 110 K). (*B*) The fraction of P features determined from the STM images obtained ∼30 min after the H_2O dose at different temperatures. The solid and dotted lines are the fits to the kinetic model. The error bars are determined based on counting statistics and at higher temperatures are within the size of the symbols used.

The temperature dependence of F_P allows us to determine the barrier for the H_2O recombination, $HO_b + HO_t \rightarrow H_2O$, by first-order kinetics (*SI Appendix*, section S2). With a prefactor of 1×10^{12} s^{-1}, the optimum fit to the data (solid line, Fig. 2*B*) yields the recombination barrier, ΔE_R = 0.355 eV. The dotted lines show the lower- and upper-bound values of 0.345 and 0.365 eV, respectively. Further, assuming equilibrium at 140 K, the value of $F_P(140K) = 0.05$ reveals that H_2O is only 0.035 eV lower in free energy than the $HO_b + HO_t$ pair.

In Fig. 3*A*, we further probe the H_2O dissociation barrier, $H_2O \rightarrow HO_b + HO_t$, in experiments where different seeding gases (neat, He, H_2) and nozzle temperatures are used to vary the H_2O incident energy (see *Methods* and further details in *SI Appendix*, section 3 and Fig. S5). At low-incident energies (< 0.3 eV), the F_P is approximately constant (∼0.05), increases above ∼0.3 eV, and reaches ∼0.35 at 1.3 eV. The observed break at ∼0.3 eV is a consequence of H_2O dissociation barrier as discussed below. Similar F_P dependence is observed for the azimuth parallel to the Ti_{5c} rows (*SI Appendix*, Fig. S6). This similarity along the two azimuths with very different corrugation of both physical and potential energy surfaces suggests that the energy dissipation may not be strongly dependent on the incident angle and exhibit so-called total energy scaling as seen previously on corrugated MgO(001) (32).

To understand the origin of the observed incident energy and temperature dependence of F_P, we perform ab initio molecular dynamics (AIMD) studies of H_2O collisions with a stoichiometric TiO_2(110). We note that extensive conformational sampling of molecularly bound H_2O resulted in only a single stable binding configuration indicating that the P features are not the result of an alternate metastable binding configuration. We start with a sample (100–200) of thermalized water configurations (T = 300 K) uniformly distributed at ∼7 Å above the surface (*SI Appendix*, Fig. S7). We add translational kinetic energy, E_K = 0.1, 0.4, 0.7, and 1.3 eV with velocities in the direction concurrent with the experiment. We propagate each trajectory until the molecules collide with the surface and dissipate their excess energy; see *SI Appendix*, section S5 for details. This procedure reproduces both the types and relative populations of species observed in the experiments, as reported in Fig. 3*A* (red squares) and *SI Appendix*, Table S1.

From the AIMD trajectories we observe the following: (*i*) At all incident energies, the fate of the species is determined by its collision point: those that land on the Ti_{5c} sites dissociate and remain adsorbed, whereas the rest are scattered. In general, at low E_K there is a pronounced steering toward the Ti_{5c} sites due to electrostatic attraction; hence, the overall number of retained species is highest at low energies. (*ii*) Irrespective of their fate after the collision, all of the molecules experience a reorientation as they approach the surface such that one OH bond is approximately perpendicular to the surface normal (Fig. 3*A*, *Inset*). This reorientation is the result of large, nonuniform electrostatic fields radiating out from the surface, coupling to the OH-bond dipole at distances ∼6 Å, that orient the molecules before impact. We note that this reorientation breaks the twofold degeneracy associated with the water binding configuration, as discussed in more detail in *SI Appendix*, section S5. (*iii*) The torquing of the molecules induces coupling of the translational/rotational/vibrational modes and amplifies the kinetic energy transfer to the water OH-bond–stretching mode. The number of events leading to bond breaking steadily increases with E_K, and those that do break have on average a higher OH-bond kinetic energy, E_{OH}. Even for the lowest E_K = 0.1 eV, there is a finite dissociation probability (∼5%) as a consequence of the steering of molecules into the bound state.

This long-range electrostatic coupling seen here for an oxide is distinct from metals and has consequences for how one can extract meaningful chemistry from molecular beam data. To generalize the interpretation of the E_K-dependent product cross-section, we note that this energy transfer effectively raises the temperature of the OH mode, and the resulting velocity distribution at the collision point can be represented by a Boltzmann distribution. AIMD trajectories resulting in OH bond breaking contribute to the long tail of $P(E_{OH}, E_K)$ (Fig. 3*B*, blue line). To assess the probability, $P_D(E_{OH})$, of whether or not a molecularly adsorbed species with E_{OH} will break, we fit the reaction coordinate (Fig. 2*B*) to a classical electrostatic potential (see *SI Appendix*, section S6 for details) and simulate an ensemble of events. The resulting $P_D(E_{OH})$ (Fig. 3*C*) is well-described by a Fermi function, as a result of the existence of well-defined energy barrier. We can combine these factors into a probability describing the OH-bond–breaking process:

$$P_D(E_K) = \int P(E_{OH}, E_K) * P_D(E_{OH}) dE_{OH}. \quad [1]$$

This model accurately reproduces the results of the AIMD trajectories as shown in Fig. 3 and *SI Appendix*, Fig. S17. This approach allows us to decouple the vibrational excitation probability, $P(E_{OH}, E_K)$, from the bond-dissociation event probability, $P_D(E_{OH})$. Whereas $P(E_{OH}, E_K)$ depends solely on electrostatics and is well-described by density-functional theory (DFT), the latter, $P_D(E_{OH})$, is associated with the potential energy landscape. Therefore, we fit the experimental data using Eq. **1** and obtain a barrier height of $E_D = 0.36 \pm 0.01$ eV (Fig. 3*A*, red line), only ∼0.04 eV lower than that obtained from DFT. Inclusion of quantum and isotopic effects is further discussed in *SI Appendix*,

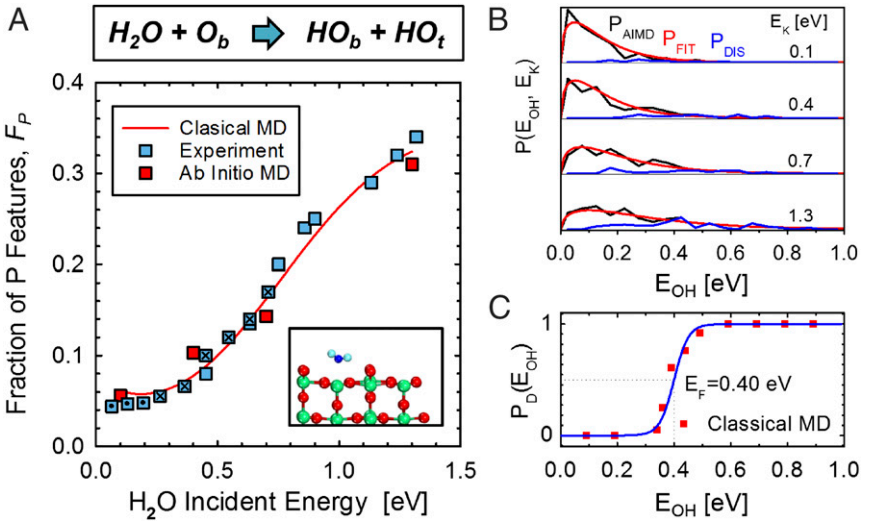

Fig. 3. (*A*) Water incident energy dependent fraction of P features, F_P, determined experimentally (blue squares) and theoretically (red squares, DFT AIMD trajectories). Seeding-gas-dependent data are coded by the square fill (neat H_2O, dot; He-seeded, cross; and H_2-seeded, empty). The red line is the fit to Eq. **1** yielding the dissociation barrier of 0.36 ± 0.01 eV. (*Inset*) Schematic shows that the water molecule is oriented with an OH bond parallel to the surface. (*B*) The distribution of OH-bond kinetic energies $P(E_{OH}, E_k)$ at the collision obtained from AIMD (black line) and a fit to a Boltzmann distribution (red). Distribution for a subset of trajectories resulting in OH bond breaking (blue). (*C*) The probability of OH-bond dissociation $P_D(E_{OH})$ as a function of OH-bond kinetic energy as estimated from an ensemble of classical MD trajectories on the DFT potential energy surface.

section S7, providing a DFT estimate of a zero-point energy-corrected barrier E_D = 0.24 eV, which is below that of experiment by 0.12 eV. The analysis presented in *SI Appendix*, section S7 implies that the system is near the cross-over between the classical and quantum regimes at the experimental temperatures.

The complete energy diagram describing the equilibrium of water deprotonation on TiO_2(110) determined from our studies is shown in Fig. 4. These unique, site-specific experiments provide a direct measure of the acid/base properties of water on an oxide surface. A combination of different computational approaches unravels the mechanism and underlying physical principles leading to water dissociation. We reveal the surprising role of long-range electrostatics in the energy transfer and redistribution before collision with the surface. We further distill a simple and meaningful theoretical framework for the interpretation of the kinetic energy dependence of scattering cross-sections. This study provides a blueprint for extracting chemical insight from supersonic beam studies of oxide surfaces and provides energetic quantification of important surface reactions relevant to catalytic materials and environmental processes.

Methods

Experimental Setup. Experiments were carried out in an Omicron low-temperature scanning tunneling microscope (LT-STM) system, which consists of a preparation chamber, microscopy chamber, and molecular beam chamber. The system is equipped with LT-STM/AFM, XPS, UV photoelectron spectroscopy, and low-energy electron diffraction. The TiO_2(110) sample (Princeton Scientific) was mounted on a standard Omicron Ta sample holder. The sample was cleaned by repeated cycles of Ne^+ sputtering and annealing up to 900–950 K. Auger electron spectroscopy was used to determine the presence of impurities on the sample surface. The concentration of V_Os on the surface determined from the images was 15%. Electrochemically etched and UHV-annealed tungsten tips were used for imaging. In all STM experiments, H_2O coverage was kept very low (~0.05 ML) to keep the observed molecules isolated. All STM images were recorded in constant-current mode at a positive sample bias of 1.2–1.6 V and tunneling currents of 5–80 pA. Based on the information from the manufacturer, the reported TiO_2 sample temperatures can be up to 3 K higher during counter heating (> 80 K) than the real sample temperatures.

Deionized H_2O was purified by several freeze–pump–thaw cycles using liquid nitrogen and dosed on TiO_2(110) directly in the STM stage with the molecular beam incident at 60° with respect to the surface normal. Experiments were carried out at different two azimuths pointing along and across the Ti_{5c} and O_b rows. Both quasi-effusive and supersonic molecular beams were used for water deposition. The neat H_2O beam was created by expanding 20 torr of water through a 50-μm orifice. The supersonic beams were produced by passing 500 torr of either helium or hydrogen through a water bubbler at room temperature and expanding the resulting mixture through a 50-μm orifice. A heatable nozzle assembly (300–900 K) was used to vary the energy of the incident H_2O. Further details are provided in *SI Appendix*, section S3.

Computational Details. All DFT calculations were performed using the CP2K package (33). The exchange-correlation energy was described by the generalized gradient approximation with the spin-polarized Perdew–Burke–Ernzerhof functional (34). The wave functions were expanded in optimized double-ζ Gaussian basis sets (35) and the plane waves were expanded with a cutoff energy of 400 Ry. Core electrons have been modeled by scalar relativistic norm-conserving pseudopotentials with 12, 4, and 1 valence electrons for Ti, O, and H, respectively (36). Brillouin zone integration is performed with a reciprocal space mesh consisting of only the Γ-points. The TiO_2(110)-p(6 × 2) surface was used to model the TiO_2 substrate, consisting of 6 O–Ti–O trilayers (18 atomic layers), and only the bottom Ti atomic layer was frozen while the remaining layers were allowed to relax. The slab was repeated periodically with a vacuum depth of ~20 Å in the direction of the surface normal. The dependence of water dissociation equilibrium on the parameters and methods of the calculations has been discussed in detail elsewhere (13, 37).

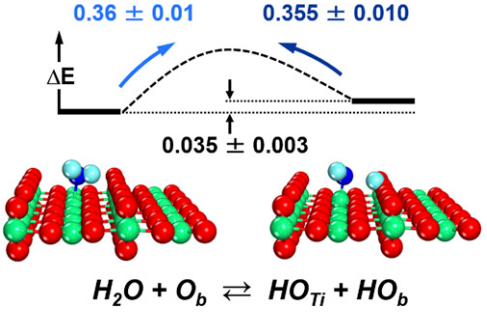

Fig. 4. Values determined for the water deprotonation potential energy surface (in electron volts) on TiO_2(110).

All AIMD simulations were performed by sampling initial conditions using a canonical [constant number, volume, temperature (NVT)] ensemble using Nosé–Hoover thermostats (38, 39) with a time step 0.5 fs. The collision simulations were performed within the microcanonical [constant number, volume, energy (NVE)] ensemble. The temperature of the TiO_2 substrate is set as 10 K and the initial translational kinetic energy of water, E_K, is chosen to be 0.1, 0.4, 0.7, and 1.3 eV, respectively, consistent with the range of beam energies in the experiments. To be comparable with the experiments, we started the simulation with a H_2O molecule in the gas phase, initially located at ∼7 Å above the surface, with a velocity at 60° to the surface normal and perpendicular to the O_b rows. We used 208 independent runs at $E_K = -0.1$ eV due to the relatively low percentage of dissociated water seen in the experimental studies at low E_K values and 104 for $E_K = 0.4$, 0.7, and 1.3 eV; each run was propagated for a total time of 1–3 ps. A total of ∼1 ns of combined AIMD trajectories was performed and used for the data analysis presented in *SI Appendix*, section S2.

For characterizing the potential energy surface of the water dissociation event, the location and energy of the transition state was performed using the climbing image nudged-elastic-band method (40) including 16 replicas. The convergence criterion for the maximum forces on the atoms is set as 2×10^{-3} a.u. The vibrational analysis was further used to confirm the transition states with only one imaginary frequency.

ACKNOWLEDGMENTS. We thank Bruce D. Kay and Charles T. Campbell for fruitful discussions. This work was supported by the US Department of Energy (DOE), Office of Basic Energy Sciences, Division of Chemical Sciences, Geosciences & Biosciences under Grant KC0301050-47319 and performed in Environmental Molecular Sciences Laboratory, a national scientific user facility sponsored by the DOE's Office of Biological and Environmental Research and located at Pacific Northwest National Laboratory (PNNL). PNNL is a multiprogram national laboratory operated for the DOE by Battelle.

1. Feibelman PJ (2010) The first wetting layer on a solid. *Phys Today* 63(2):34–39.
2. Maier S, Salmeron M (2015) How does water wet a surface? *Acc Chem Res* 48(10): 2783–2790.
3. Henderson MA (2002) The interaction of water with solid surfaces: Fundamental aspects revisited. *Surf Sci Rep* 46(1-8):1–308.
4. Carrasco J, Hodgson A, Michaelides A (2012) A molecular perspective of water at metal interfaces. *Nat Mater* 11(8):667–674.
5. Ma M, Tocci G, Michaelides A, Aeppli G (2016) Fast diffusion of water nanodroplets on graphene. *Nat Mater* 15(1):66–71.
6. Saavedra J, Doan HA, Pursell CJ, Grabow LC, Chandler BD (2014) The critical role of water at the gold-titania interface in catalytic CO oxidation. *Science* 345(6204): 1599–1602.
7. Rausch B, Symes MD, Chisholm G, Cronin L (2014) Decoupled catalytic hydrogen evolution from a molecular metal oxide redox mediator in water splitting. *Science* 345(6202):1326–1330.
8. He Y, Tilocca A, Dulub O, Selloni A, Diebold U (2009) Local ordering and electronic signatures of submonolayer water on anatase TiO_2(101). *Nat Mater* 8(7):585–589.
9. Shin H-J, et al. (2010) State-selective dissociation of a single water molecule on an ultrathin MgO film. *Nat Mater* 9(5):442–447.
10. Eng PJ, et al. (2000) Structure of the hydrated α-Al_2O_3 (0001) surface. *Science* 288(5468):1029–1033.
11. Merte LR, et al. (2012) Water-mediated proton hopping on an iron oxide surface. *Science* 336(6083):889–893.
12. Hu XL, Carrasco J, Klimeš J, Michaelides A (2011) Trends in water monomer adsorption and dissociation on flat insulating surfaces. *Phys Chem Chem Phys* 13(27):12447–12453.
13. Mu R, et al. (2014) Dimerization induced deprotonation of water on RuO_2(110). *J Phys Chem Lett* 5(19):3445–3450.
14. Henderson MA (2011) A surface science perspective on TiO_2 photocatalysis. *Surf Sci Rep* 66(6-7):185–297.
15. Diebold U (2003) The surface science of titanium dioxide. *Surf Sci Rep* 48(5-8):53–229.
16. Pang CL, Lindsay R, Thornton G (2013) Structure of clean and adsorbate-covered single-crystal rutile TiO_2 surfaces. *Chem Rev* 113(6):3887–3948.
17. Dohnalek Z, Lyubinetsky I, Rousseau R (2010) Thermally-driven processes on rutile TiO_2(110)-(1 x 1): A direct view at the atomic scale. *Prog Surf Sci* 85(5-8):161–205.
18. Wendt S, et al. (2006) Formation and splitting of paired hydroxyl groups on reduced TiO_2(110). *Phys Rev Lett* 96(6):066107.
19. Du Y, et al. (2009) Two pathways for water interaction with oxygen adatoms on TiO_2(110). *Phys Rev Lett* 102(9):096102.
20. Walle LE, Borg A, Uvdal P, Sandell A (2009) Experimental evidence for mixed dissociative and molecular adsorption of water on a rutile TiO_2(110) surface without oxygen vacancies. *Phys Rev B* 80(23):235436.
21. Kimmel GA, et al. (2012) Polarization- and azimuth-resolved infrared spectroscopy of water on TiO_2(110): Anisotropy and the hydrogen-bonding network. *J Phys Chem Lett* 3(6):778–784.
22. Duncan DA, Allegretti F, Woodruff DP (2012) Water does partially dissociate on the perfect TiO_2(110) surface: A quantitative structure determination. *Phys Rev B* 86(4): 045411.
23. Brookes IM, Muryn CA, Thornton G (2001) Imaging water dissociation on TiO_2(110). *Phys Rev Lett* 87(26):266103.
24. Matthiesen J, et al. (2009) Formation and diffusion of water dimers on rutile TiO_2(110). *Phys Rev Lett* 102(22):226101.
25. Lee J, Sorescu DC, Deng X, Jordan KD (2013) Water chain formation on TiO_2(110). *J Phys Chem Lett* 4(1):53–57.
26. Jensen JA, Yan C, Kummel AC (1995) Energy dependence of abstractive versus dissociative chemisorption of fluorine molecules on the silicon (111)-(7x7) surface. *Science* 267(5197):493–496.
27. Smerieri M, Reichelt R, Savio L, Vattuone L, Rocca M (2012) Coupling scanning tunneling microscope and supersonic molecular beams: A unique tool for in situ investigation of the morphology of activated systems. *Rev Sci Instrum* 83(9):093703.
28. Wiggins B, Avila-Bront LG, Edel R, Sibener SJ (2016) Temporally and spatially resolved oxidation of Si(111)-(7 × 7) using kinetic energy controlled supersonic beams in combination with scanning tunneling microscopy. *J Phys Chem C* 120(15):8191–8197.
29. Hundt PM, Jiang B, van Reijzen ME, Guo H, Beck RD (2014) Vibrationally promoted dissociation of water on Ni(111). *Science* 344(6183):504–507.
30. Killelea DR, Campbell VL, Shuman NS, Utz AL (2008) Bond-selective control of a heterogeneously catalyzed reaction. *Science* 319(5864):790–793.
31. Smith RR, Killelea DR, DelSesto DF, Utz AL (2004) Preference for vibrational over translational energy in a gas-surface reaction. *Science* 304(5673):992–995.
32. Dohnalek Z, Smith RS, Kay BD (2002) Adsorption dynamics and desorption kinetics of argon and methane on MgO(100). *J Phys Chem B* 106(33):8360–8366.
33. VandeVondele J, et al. (2005) QUICKSTEP: Fast and accurate density functional calculations using a mixed Gaussian and plane waves approach. *Comput Phys Commun* 167(2):103–128.
34. Perdew JP, Burke K, Ernzerhof M (1996) Generalized gradient approximation made simple. *Phys Rev Lett* 77(18):3865–3868.
35. VandeVondele J, Hutter J (2007) Gaussian basis sets for accurate calculations on molecular systems in gas and condensed phases. *J Chem Phys* 127(11):114105.
36. Goedecker S, Teter M, Hutter J (1996) Separable dual-space Gaussian pseudopotentials. *Phys Rev B Condens Matter* 54(3):1703–1710.
37. Kumar N, Kent PRC, Wesolowski DJ, Kubicki JD (2013) Modeling water adsorption on rutile (110) using van der Waals density functional and DFT+U methods. *J Phys Chem C* 117(45):23638–23644.
38. Nosé S (1984) A unified formulation of the constant temperature molecular dynamics methods. *J Chem Phys* 81(1):511–519.
39. Hoover WG (1985) Canonical dynamics: Equilibrium phase-space distributions. *Phys Rev A Gen Phys* 31(3):1695–1697.
40. Henkelman G, Uberuaga BP, Jonsson H (2000) A climbing image nudged elastic band method for finding saddle points and minimum energy paths. *J Chem Phys* 113(22): 9901–9904.